Journal of Magnetic Resonance 198 (2009) 80–87

Contents lists available at ScienceDirect

Journal of Magnetic Resonance

journal homepage: www.elsevier.com/locate/jmr

Mobile sensor for high resolution NMR spectroscopy and imaging

Ernesto Danieli, Jörg Mauler, Juan Perlo, Bernhard Blümich, Federico Casanova *

Institut für Technische Chemie und Makromolekulare Chemie, RWTH Aachen University, Worringerweg 1, D-52074 Aachen, Germany

ARTICLE INFO

Article history:
Received 31 October 2008
Revised 13 January 2009
Available online 25 January 2009

Keywords:
Halbach array
MRI
Mobile NMR
Permanent magnet
NMR spectroscopy

ABSTRACT

In this work we describe the construction of a mobile NMR tomograph with a highly homogeneous magnetic field. Fast MRI techniques as well as NMR spectroscopy measurements were carried out. The magnet is based on a Halbach array built from identical permanent magnet blocks generating a magnetic field of 0.22 T. To shim the field inhomogeneities inherent to magnet arrays constructed from these materials, a shim strategy based on the use of movable magnet blocks is employed. With this approach a reduction of the line-width from ~20 kHz to less than 0.1 kHz was achieved, that is by more than two orders of magnitude, in a volume of 21 cm^3. Implementing a RARE sequence, 3D images of different objects placed in this volume were obtained in short experimental times. Moreover, by reducing the sample size to 1 cm^3, sub ppm resolution is obtained in ^{1}H NMR spectra.

1. Introduction

The common practice of NMR involves the use of large magnets with strong and homogeneous magnetic fields suitable to obtain information about spatial distributions, molecular structure and molecular dynamics for a wide range of materials. For many applications, however, it would be useful to carry out magnetic resonance spectroscopy and imaging on small mobile NMR devices. Portable NMR probes built from permanent magnets offer several advantages over conventional NMR systems [1,2]. They are small in size, low in cost and robust. Among the different magnet geometries available, the cylindrical Halbach array [3] is particularly convenient because it generates a comparatively strong magnetic field at a relatively large bore size for positioning the sample. Moreover, it generates a magnetic field transverse to the longitudinal axis of the magnet bore, allowing the use of sensitive solenoids as radiofrequency coils. Although in theory, this magnet geometry is expected to provide a rather homogeneous field, in practice, the inhomogeneity of the magnetic material, and the inaccuracy in the size and positioning of the magnet pieces in the final array lead to significant field distortions [4–8]. Typical values of the field inhomogeneities are some tens of kHz, prohibiting the use of established techniques for high-resolution spectroscopy and imaging.

We have recently shown that shim units built from movable permanent magnet blocks can be implemented to control the homogeneity of the stray magnetic field in single-sided NMR [9,10]. In a first approach we demonstrated that movable permanent magnet blocks can be used to match the inhomogeneous B_0 field generated by an open magnet to the inhomogeneity generated by an adapted surface rf coil [9]. By combining nutation of the magnetization in the B_1 field with precession in the B_0 field it was possible to recover spectroscopic information with a genuine one-sided NMR sensor. More recently, this approach has proven to provide sufficient control to shim the stray field of a single-sided magnet to sub ppm homogeneity allowing the measurements of ^{1}H chemical shift resolved spectra by single-pulse excitation [10].

In this work we report the construction of a mobile tomograph by exploiting the concept of movable permanent magnets in the shim unit of a Halbach array. In particular, we show that by using four pairs of small blocks placed inside the magnet bore the field inhomogeneity can be reduced to the theoretical limit expected from field calculations. In a cylindrical volume 30 mm in diameter and 30 mm long, the line-width was improved from 20 kHz down to 0.1 kHz allowing the use of conventional MRI techniques. Furthermore, sub ppm spectral resolution was achieved in a volume of about 1 cm^3.

2. Magnet array

The ideal Halbach magnet (Fig. 1a) requires a polarization varying in a continuous way along the circumference to generate the optimum magnetic field in terms of strength and homogeneity. For practical reasons of construction, however, one has to resort to a discrete approximation of a Halbach magnet that is a Halbach array (Fig. 1b–c) [3,5]. The Mandhala array [5] (Fig. 1c) is a particularly convenient discretization which consists of identical magnet pieces. We built the main Halbach magnet from six stacked Mandhala rings. The rings are arranged in two groups separated by a central gap d_z^{main} included to compensate for axial field distortions

* Corresponding author. Fax: +49 241 8022185.
E-mail address: fcasanova@mc.rwth-aachen.de (F. Casanova).

1090-7807/$ - see front matter © 2009 Elsevier Inc. All rights reserved.
doi:10.1016/j.jmr.2009.01.022

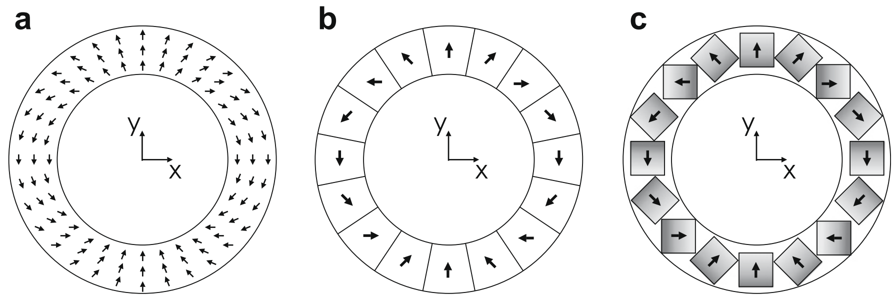

Fig. 1. (a) Ideal Halbach magnet in which the polarization varies continuously along the ring circumference. (b) Discrete approximation in terms of a Halbach array built from pieces polarized in different directions. (c) Scheme of one Mandhala ring. Six of such rings were stacked to build the main magnet unit used in this work. The arrows indicate the polarization direction of each permanent magnet. The x and y axes of the Cartesian coordinate system are centred with the magnet where y points along the direction of the magnetic field. The z axis (not shown) points out of the page.

due to the finite length of the magnet. The region of interest is a cylindrical volume centered within this magnet. The orientation of the magnetic field, which unlike traditional superconducting magnets is perpendicular to the ring axis, defines the y direction of our reference system, while z points along the direction of the bore.

2.1. Spatial dependence of the main magnetic field

The first attempt to optimize the field homogeneity in the working volume is to adjust the gap of the main unit d_z^{main} properly. In order to gain some insight into the dependence of the magnetic field on d_z^{main}, the ideal magnetic field profile is first analyzed for a vanishing gap. Due to the symmetry of the magnet array, the spatial dependence of the field is characterized by even terms in its Taylor expansion around $\vec{r}_0 = (0,0,0)$. The magnetic field magnitude varies differently in different directions. For example, along x and y, the field is shaped like an arms-up parabola increasing its magnitude as the permanent magnets blocks are approached. This is mainly due to the dependence of the field on the inverse of the distance to the magnetic source. On the other hand, along z, the field decreases like an arms-down parabola when moving away of the centre as a consequence of the finite size of the magnet along the axial direction (Fig. 2a).

However, with increasing gap width the curvature of the magnetic field at the origin can be decreased and even inverted so that the field along the z-axis eventually varies like an arms-up parabola, and along x and y like arms-down parabolas (Fig. 2b). The behavior shown in Fig. 2a and b suggests that there must be a particular gap $d_{z,opt}^{main}$ for which the transition from arms-up to arms-down parabola is produced. From the simulations it can be seen that the zero cross of all three quadratic coefficients is obtained for the same $d_{z,opt}^{main}$ (Fig. 2c). Then, this separation length is the optimum concerning homogeneity, since adjusting the gap at this position leads to a uniform field along all directions.

Although a homogeneous field is expected in theory for the optimum gap, experimentally it is by far not achieved. This is so because the symmetry invoked above is violated when using real magnet pieces. For instance, the inhomogeneity of the magnetic material, the inaccuracy in the size of the pieces and even the errors when positioning the pieces in the final array, lead to considerable field distortions, including linear spatial dependences, which cannot be corrected just by adjusting the gap d_z^{main}. To shim the complex spatial dependence of the magnetic field of a Halbach array made from imperfect magnet pieces, more variables of control are needed than just an adjustable central gap.

In order to design a suitable shim system, it is necessary to identify and quantify the inhomogeneities of the magnetic field generated by the Halbach array. For this purpose a formal description of the spatial variations of the magnetic field needs to be introduced. The behavior of the magnetic field within the working volume (current-free region) is governed by the Laplace equation

$$\left(\frac{d^2}{dx^2} + \frac{d^2}{dy^2} + \frac{d^2}{dz^2}\right)\vec{B}_0(\vec{r}) = 0. \quad (1)$$

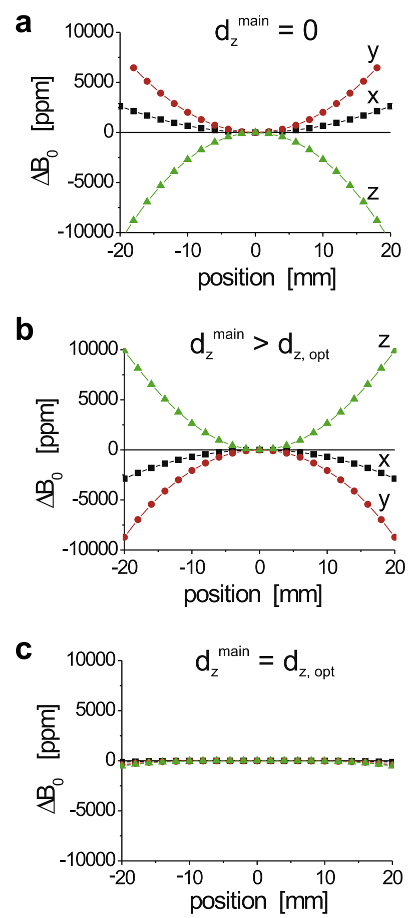

Fig. 2. Spatial dependence of the magnetic field along the three Cartesian directions calculated for a main gap d_z^{main} (a) smaller than, (b) larger than, and (c) equal to the optimum value $d_{z,opt}^{main}$. The simulations correspond to a magnet built from two Halbach rings made of 16 blocks 40 × 40 × 160 mm^3 arranged in the xy plane with the long axis along z following Ref. [5]. Using these dimensions for the pieces internal and external radios of R_{in} = 100 mm and R_{out} = 160 mm are defined. For this array we found $d_{z,opt}^{main}$ = 21 mm.

It is a consequence of Maxell's equations $\nabla \cdot \vec{B} = 0$ and $\nabla \times \vec{B} = 0$. Although Eq. (1) is satisfied by the three components of the total field $\vec{B}_0$, in the present case it is sufficient to consider the equation for the y component B_{0y}, since $|B_{0x}|, |B_{0z}| << |B_{0y}|$ and can be neglected. Then, from now on we will refer to the magnetic field as $B_0 \equiv B_{0y}$. The solution of Eq. (1) is usually expressed in terms of an expansion in spherical harmonic functions [11]. In the present analysis we express these functions in Cartesian coordinates because they are adapted to the geometry of the described magnet as will be seen later. Up to second order, the spatial dependence of the field can formally be expressed as

$$\begin{aligned} B_0(\vec{r}) &= B_{00} + \Delta B_0(\vec{r}) \\ &= C_0 + C_{11+}x + C_{11-}y + C_{10}z + C_{20}(2z^2 - x^2 - y^2) + C_{22+}(x^2 - y^2) \quad (2) \\ &+ C_{22-}xy + C_{21+}xz + C_{21-}yz + o(r^3)\ldots \end{aligned}$$

where the coefficients $C_{nm\pm}$ make reference to the symmetric and antisymmetric combinations of the spherical harmonics $(Y_n^m(x,y,z) \pm Y_n^{-m}(x,y,z))$ of order n and degrees $+m$ and $-m$. In Eq. (2) the homogeneous contribution to the field comes only from the first term C_0 of the right hand side, while the remaining terms represents the field inhomogeneity. We carried the expansion up to second order as these terms are expected to describe the main source of inhomogeneity that we aim to remove in this work. In order to quantify the homogeneity of the magnet through the magnitude of $\Delta B_0(\vec{r})$, it is mandatory to scan the magnetic field and extract the values of the coefficients C_{nm} ($n = 1,2$; $m \leq n$) in Eq. (2). This information is then used to design the shim unit.

3. Shim unit

A standard and robust approach to adjust the magnetic field for high resolution in conventional NMR magnets uses shim coils that generate fields with known spatial dependences [12]. An alternative shim approach was experimentally demonstrated using movable permanent magnet blocks to locally adjust the highly inhomogeneous stray field of a single sided sensor [10]. On one hand the permanent polarization of the magnet blocks provides the equivalent of about 1000 A DC current without a power supply, but on the other hand the current value cannot be changed like in conventional shim systems. Nevertheless, proper mechanical movement of such magnet blocks can generate adjustable shim fields.

The shim unit is specially designed to match the spatial dependency of the magnetic field generated by the main Halbach array and will work only in combination with it. This means that detailed knowledge of the main magnetic field properties is required for designing the shim unit. This information is used to obtain, by numerical calculations, the dimensions and optimum or equilibrium position of the magnet blocks forming the shim unit. The magnet blocks must be free to move around the optimum positions in order to permit final corrections, which are related to the inhomogeneities of the shim magnets themselves (polarization, size and positioning inaccuracies). In this way one can experimentally reach the performance calculated numerically for the Halbach array.

The field generated by the shim unit must reproduce the spatial dependence of the main field and have the smallest average field strength possible. By setting the polarization of the shim unit opposite to that of the main field, the inhomogeneities of the last are corrected while the total field strength is maintained at an acceptable magnitude. Another aspect to take into account when designing the shim unit is the range within which each magnet of the shim unit needs to move to generate the required spatial corrections. This range must be smaller than the size of the working volume because otherwise unwanted higher order terms in the field expansion are generated when the magnet pieces are far away from their equilibrium positions. On the other hand, assuming a certain precision in the movements can be achieved, the range should be large enough to provide reasonable control at the time of generating the required magnetic field terms. In order to satisfy these requirements and in correspondence with the main unit, the shim unit consists also of two Halbach rings separated by a gap d_z along the z-axis (Fig. 3a). Each of these rings is formed by four permanent magnets, which constitutes the simplest Halbach ring. The small number of pieces in each ring generates a low field and

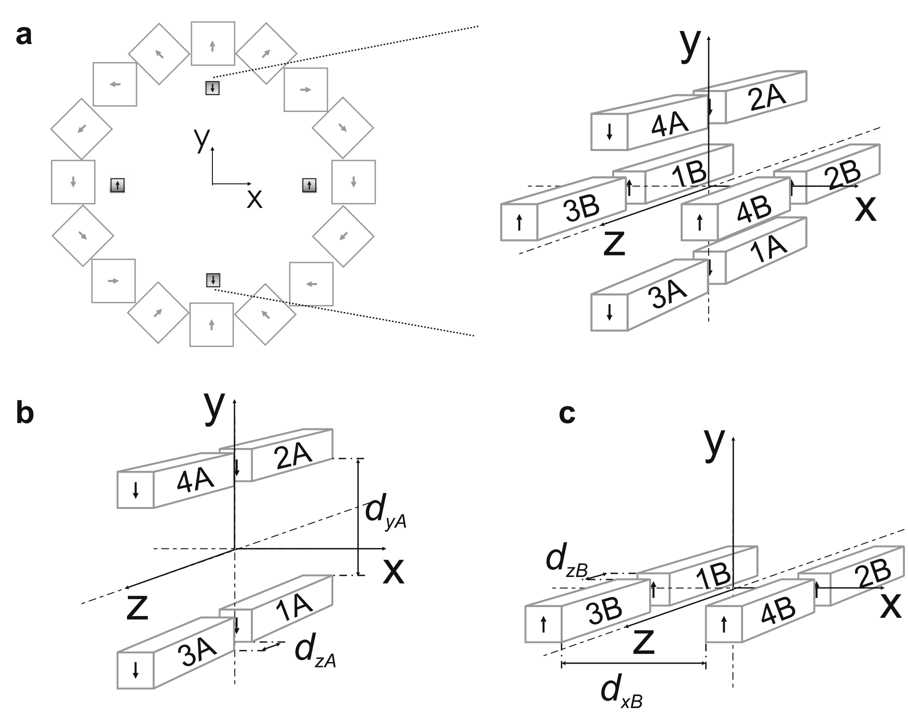

Fig. 3. (a) Schematic representation of the shim unit consisting of two Halbach rings each composed of four magnets. To better identify the movements of the magnets required to generate the shim terms, the Halbach rings are split in two groups. Group A includes the four magnets lying in the yz plane (b) and group B the four lying in the xz plane (c). The independent movement of the magnets within these groups improves the performance of the shim unit.

provides the required number of control variables necessary to generate the shim corrections up to second order.

In order to simplify the description of the movements required to obtain the shim terms, the permanent magnets were grouped into two sets A and B of magnets (Fig. 3). Group A contains the four magnets that lie in the *yz* plane (Fig. 3b) and the group B is formed by the four magnets lying in the *xz* plane (Fig. 3c). By moving the pieces independently in each group it is possible to remove inhomogeities of the magnetic field up to second order. Table 1 shows the combinations of displacements along different directions Δk ($k = x$, y, and z) of the individual magnets to generate corrections proportional to each of the terms of Eq. (2). For a detailed description of the principle of the shim unit see [13].

4. Experimental

The Halbach array was built from six Mandhala rings, each composed of 16 identical magnet blocks [5] (Fig 1c). The rings were separated into two groups each of them made by stacking three Halbach rings. Each magnet block of $40 \times 40 \times 40$ mm^3 was made from a NdFeB alloy with a remnant flux density of 1.33 T, coercive field strength of 796 kAm^{-1}, and a temperature coefficient of -1200 ppm/°C. Since the remnant magnetization of permanent magnets varies a few percent between pieces, the field of each piece was carefully measured and a polarization histogram was build. The magnets were sorted by placing those with smaller deviation from the center of the distribution in the inner rings and those with larger deviations in the outer rings. This selection procedure can be further improved by calculating permutations between magnet blocks [14]. The final Halbach array, including the aluminum holder, has an outer diameter of 330 mm, a length of 270 mm and a weight of approximately 50 Kg. The magnet bore is 200 mm and the average field strength 0.22 T.

To excite and detect NMR signals from a volume 50 mm in diameter and 50 mm in length, a solenoid rf coil of seven windings was built with a diameter of 50 mm and a length of 120 mm. Using an output power of 150 W the duration of the 180° hard-pulse was about 20 μs. The magnet was equipped with a three-axis gradient coil system to provide the sensor with imaging capabilities in this volume (see Fig. 4). The gradients G_x and G_y along x and y, are generated by quadrupolar coils [15] (Fig. 4a–b). They are 90 mm in diameter and 120 mm long. The gradient G_z, along the direction z of the magnet axis, is produced by two paired saddle coils each of them 90 mm in diameter and 70 mm in length, separated by a 38 mm gap along the z axis (Fig. 4c). As the set of three gradient coils surrounds the rf coil, a shielding made of thin cupper strips was positioned between the gradient and rf coils to avoid coupling between them and to reduce external noise from the audio amplifiers. The coil efficiencies are 0.0056 Tm^{-1} A^{-1} for the quadrupolar coils (x and y directions) and 0.004 Tm^{-1} A^{-1} for the pair of saddle coils. The gradient coils were driven with three Tecron amplifiers LV5050, which deliver a maximum of 30 A at 2 Ω.

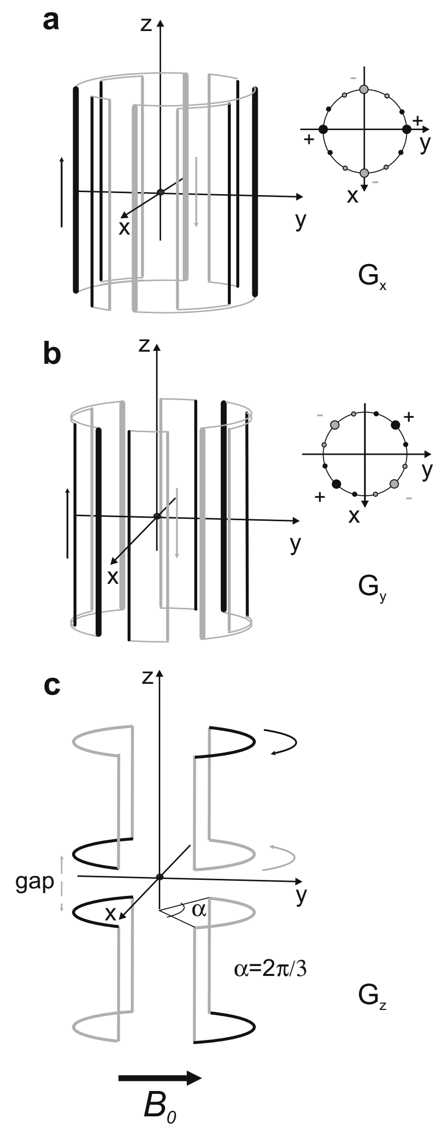

Fig. 4. 3D schemes of the coils to generate gradients along the *x*, *y*, and *z* axes. (a and b) show quadrupolar coils. The two different widths of the conductors are proportional to the current. Black lines indicate current flowing along the *z* direction (black arrow), while grey colour represents current flowing along the $-z$ direction (grey arrow). The insets to the right of both figures are cross sectional plots that indicate the current in each wire. Plus (+) and minus (−) signs indicate current flowing out and into the page. The *z* axis points out of the page. (c) Two paired saddle coils separated by a gap along the *z*-axis generate a magnetic field with a positive linear dependence along *z*. The current flows in clockwise direction in the portions coloured in black and in anti-clockwise direction in the portions coloured in grey. The direction of the main magnetic field B_0 is indicated at the bottom of the figure.

Table 1
Shim coefficients vs. spatial movements of the individual permanent magnets.

Coefficient	Spatial dependence	Magnet label							
		1A	2A	3A	4A	1B	2B	3B	4B
C_{11+}	x	$-\Delta x$	$-\Delta x$	$-\Delta x$	$-\Delta x$	Δx	Δx	Δx	Δx
C_{11-}	y	$-\Delta y$	$-\Delta y$	$-\Delta y$	$-\Delta y$	Δy	Δy	Δy	Δy
C_{10}	z	Δz	Δz	Δz	Δz	Δz	Δz	Δz	Δz
C_{21+}	xz	$-\Delta x$	$-\Delta x$	Δx	Δx	$-\Delta x$	$-\Delta x$	Δx	Δx
C_{21-}	yz	$-\Delta y$	$-\Delta y$	Δy	Δy	$-\Delta y$	$-\Delta y$	Δy	Δy
C_{22-}	xy	$-\Delta x$	Δx	$-\Delta x$	Δx	$-\Delta x$	Δx	$-\Delta x$	Δx
C_{22+}	x^2-y^2	Δz	Δz	$-\Delta z$	$-\Delta z$	$-\Delta x$	Δx	$-\Delta x$	Δz
C_{20}	$2z^2-x^2-y^2$	Δz	Δz	$-\Delta z$	$-\Delta z$	Δx	$-\Delta x$	Δx	$-\Delta x$

5. Results and discussion

5.1. Scanning the main magnetic field

To map the volume within the magnet center where the field is to be shimmed, a cylindrical water sample 30 mm in diameter and 50 mm long was imaged. To this end a CSI sequence like the one shown in Fig. 5a was used. It is a modified version of the one discussed in ref. [16]. The sequence consists of a selective 90° pulse followed by a train of hard 180° pulses. The soft pulse selects the desired plane, for example *xy*, *xz* or *yz* (Fig. 6). To scan the whole 2D k-space in one shot, the amplitudes of both phase encoding gradient pulses are stepped within the train of hard 180° pulses from $-G_{max}$ to G_{max} (Fig 5a). This is possible due to a moderate number of pixels used along both phase encoding directions. In this way the acquired data set consist in a 3D matrix in which two dimensions are associated to the 2D k-space and the other to the temporal domain. Following a 3DFT, the resonance frequency or line center in the spectral dimension is determined for each spatial position. This frequency maps the magnitude of the magnetic field (Fig. 6). Notice, that in this procedure, the precision to measure the field value is determined by the signal-to-noise ratio rather than the nominal resolution given by the inverse of the acquisition time. For the results shown in Fig. 6 the precision is better than 10 ppm.

Fig. 6a shows the *xy*, *xz* and *yz* field maps of the main unit obtained in this way. Within the scanned volume of 30 mm diameter and 50 mm length, the field distortions are larger than 2000 ppm

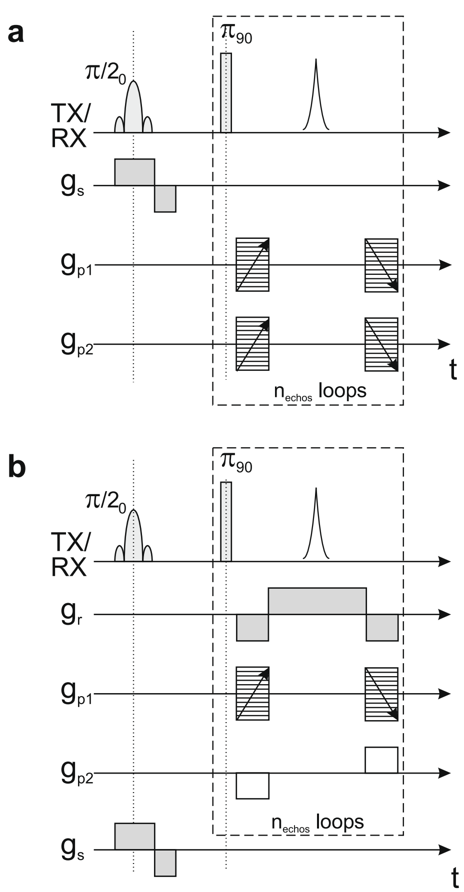

Fig. 5. (a) CSI sequence for measuring the magnetic field homogeneity. The amplitudes of both phase encoding gradient pulses are stepped from $-G_{max}$ to G_{max} in one CPMG train. (b) RARE sequence for measuring 2D and 3D images. In the last case, the g_{p2} amplitude is stepped in different scans.

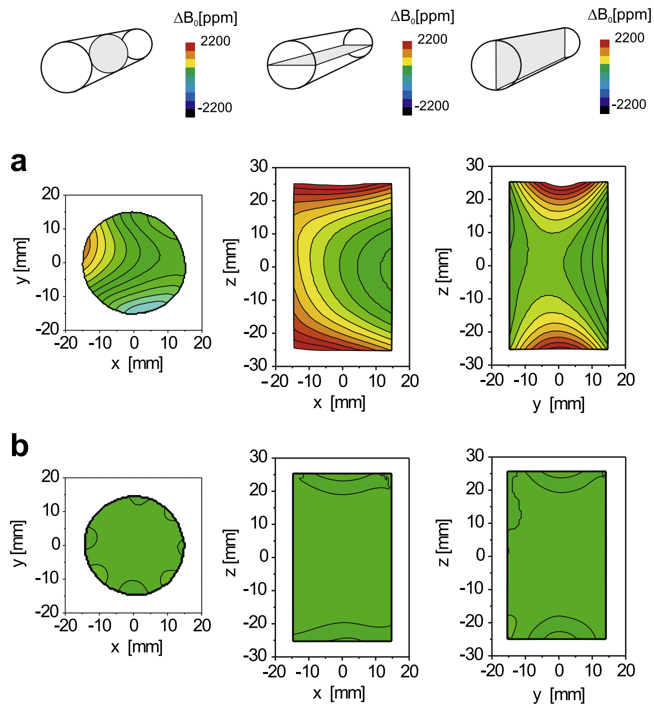

Fig. 6. (a) 2D maps of the magnetic field of the sensor without shim unit. (b) 2D field maps with shim unit. The acquisition time for one echo was t_{acq} = 0.52 ms with an echo-time of t_E = 3 ms. 16 pixel were imaged along both spatial directions. The lines in the contour plots are separated by 200 ppm covering the range indicated on the top of each map. Averaging only two scans allowed us to acquire 2D maps in a time of about 10 s.

(~20 KHz). The values of the coefficients that characterize these inhomogeneities are listed in Table 2. Since we were interested only in the determination of lower order coefficients up to order two, it was possible to implement a method simpler than the one usually employed to characterize the harmonic components of the magnetic field [17,18]. The experimental curves along the three Cartesian directions were fitted by polynomial functions to obtain the Taylor expansion coefficients of the magnetic field around the origin $\vec{r}_0 = (0,0,0)$ for each corresponding direction. These coefficients are directly related to the ones of Eq. (2), and C_{10}, C_{11-}, C_{11+}, C_{20}, and C_{22+} could be calculated. For example, by setting $x = y = 0$ in Eq. (2), one obtains a polynomial function of the field along z $B_0(z) = C_0 + C_{10}z + 2C_{20}z^2 + O(z^3)$. As this expression must coincide with the Taylor expansion along z, $C_{10} = \frac{\partial B_0(\vec{r}_0)}{\partial z}$, and $2C_{20} = \left(\frac{1}{2!}\frac{\partial^2 B_0(\vec{r}_0)}{\partial z^2}\right)$. A similar analysis for the transverse directions (x and y) yields the values for C_{20}, and C_{22+}. For the determination of cross coefficients, like C_{21+} proportional to the xz term, $y = 0$ is set in Eq. (2). By rearranging Eq. (2) one finds that the term proportional to z is $(C_{10} + C_{21+}x)z$. Combining linear fits along z for two different values of x it is possible to obtain the value of C_{21+}

Table 2
Measured coefficients of the main magnetic field corresponding to Eq. (2).

Coefficient	Spatial dependence	Measured value
C_{11+}	x	58 (ppm/mm)
C_{11-}	y	16 (ppm/mm)
C_{10}	z	2 (ppm/mm)
C_{21+}	xz	0.6 (ppm/mm^2)
C_{21-}	yz	0 (ppm/mm^2)
C_{22-}	xy	1.3 (ppm/mm^2)
C_{22+}	x^2-y^2	2.3 (ppm/mm^2)
C_{20}	$2z^2-x^2-y^2$	1 (ppm/mm^2)

independent of C_{10}. Through a similar procedure in the *xy* and *yz* planes it is possible to obtain C_{22-} and C_{21-}.

Fig. 6a and the values of Table 2 reveal that, the homogeneity of the magnetic field is altered mainly by the presence of a linear field term along the *x* direction. In the *xy* map, the displacement of the center of the magnetic field map along positive *x* and *y* values is caused by an important cross term in *xy*. The *xz* and *yz* maps of Fig. 6a, show the quadratic dependence along the *z* direction associated with the C_{20} coefficient in Table 2.

5.2. Shim procedure

The field of the main unit is used as the source field to be corrected by the shim unit. With the help of computer simulations based on the measured data of Table 2, the dimensions and positions of the shim magnets were obtained. For magnet blocks with dimensions $5 \times 10 \times 45$ mm^3, $d_{zA} = 15$ mm, $d_{yA} = 138$ mm, $d_{zB} = 12$ mm, and $d_{xA} = 144$ mm were used as the starting point. Once the NeFeB shim magnet blocks are mounted and placed at the calculated positions, an iterative procedure to obtain the final shim configuration starts. The small blocks are placed in an aluminium holder equipped with screws that allow to control the position of each individual block in all three directions with a precision better than 100 μm. The total field generated by the superposition of the main and the shim unit is scanned with the CSI sequence (Fig. 5a). Subsequently, the positions of the shim magnet pairs are adjusted to compensate the field inhomogeneities remaining from the previous correction. This procedure is repeated several times until the deviations from the average field are smaller than 10 ppm.

Fig. 6b shows the two dimensional field maps after applying this iterative procedure. The scale used to plot the magnitude of the magnetic field is the same as the one used in Fig. 6a in order to compare both results. In contrast with Fig. 6a it can be seen that in a cylindrical volume 30 mm in diameter and around 30 mm in length, the observation of field variations is limited by the scale resolution, which hides smaller field variations. The lobules found in the outer regions of the *xy* map of Fig. 6b, indicate that higher order terms (harmonics of order 4) become relevant. In order to eliminate these terms a shim unit with more magnet pieces would be needed.

To achieve a finer correction of the first order terms, the current through the gradient coils was varied in a second step until the signal peak in the frequency domain of a water sample that fully occupied the working volume was maximized. The maximum current required in the gradient coils to correct the remaining linear terms was of the order of 250 mA. Through this procedure it was also possible to characterize the magnet homogeneity by measuring the spectral line-width. Fig. 7a compares the NMR lines measured with and without the shim unit for a cylindrical water sample 30 mm long and 30 mm in diameter (~21 cm^3). The improvement achieved with the shim unit is evident. The spectral line-width is more than two orders of magnitude narrower than the one measured without the shim unit. Fig. 7b shows that by reducing the sample volume, it is possible to achieve sub ppm resolution (0.85 ppm) in a cylindrical volume 10 mm long and 10 mm in diameter (~1 cm^3). Fig. 7c shows that this homogeneity allows us to resolve the two lines corresponding to methyl and carboxylic protons of acetic acid, which appear at around 2.5 and 11.5 ppm, with an intensity ratio of 3:1. Although a frequency drift of 0.25 Hz/s associated with temperature variations of the magnet constrained the measurements to single-scan experiments, a signal-to-noise of 85 was obtained in the spectra.

5.3. 3D images

The good homogeneity achieved with the shim unit over a relatively large volume, allows us to measure 3D images free from artifacts introduced by field distortions without excessive gradient power requirements. These artifacts are geometric and intensity distortions in the image. Their relevance not only depends on the size of the working volume and the inhomogeneity of the magnetic field, but also on the method chosen to measure the images and the strength of the available gradients [19,20]. For instance, in the case of a conventional 2DFT imaging method [1,15] (the following analysis is also applicable if a RARE sequence is employed for imaging purposes), the shift Δx, in the image due to $\Delta B_0(\vec{r})$ is: $\Delta x(\vec{r}) = \frac{\Delta B_0(\vec{r})}{\gamma G_x}$, where G_x represents the gradient along the read direction. Fig. 7a reveals that the gradient needed to avoid noticeable image distortions is almost two orders of magnitude lower for the shimmed field than for the unshimmed field of the main array.

With the RARE sequence (Fig. 6b) data acquisition could be accelerated. It allowed us to measure images of 2D slices selected by means of the application of a soft 90° pulse and full 3D images. In the latter case, spatial position in the *xy* plane is encoded within one echo-train by combining a read gradient with a phase-encoding gradient which is stepped from $-G_{max}$ to G_{max} for successive echoes. This procedure is repeated for every gradient step of the second phase encoding gradient, which is set in the *z* direction (Fig. 6b). Fig. 8a shows a 3D image of a phantom made of three con-

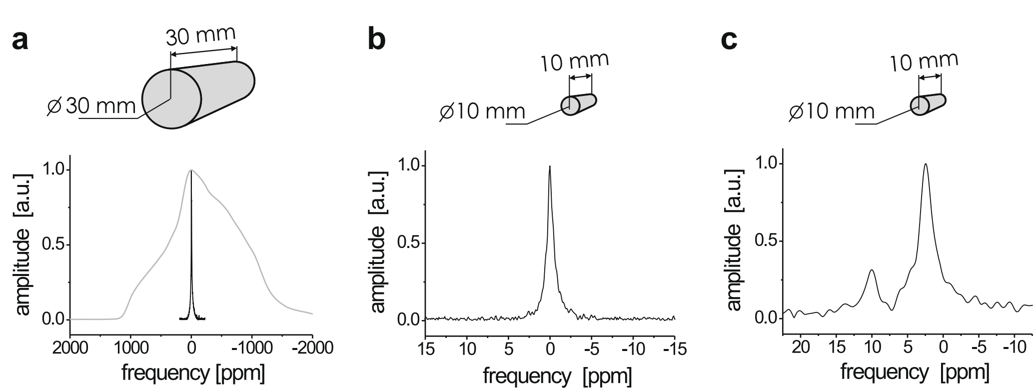

Fig. 7. (a) Line shapes measured with (black line) and without (gray line) the shim unit for a cylindrical water sample 30 mm long and 30 mm in diameter (21 cm^3). (b) Line shape of a cylindrical water sample 10 mm in diameter and 10 mm long (~1 cm^3), which demonstrates the homogeneity obtained with the shim unit in this volume. The line-width measured at half height is 0.85 ppm. (c) Magnitude spectrum of acetic acid measured for a sample of the same volume as (b). The experiments were run using a single scan to avoid line broadening due to the frequency drift (0.25 Hz/s without any temperature controller for the magnet). The spectrum is the Fourier transform of the Hahn-echo signal acquired during t_{acq}=130 ms.

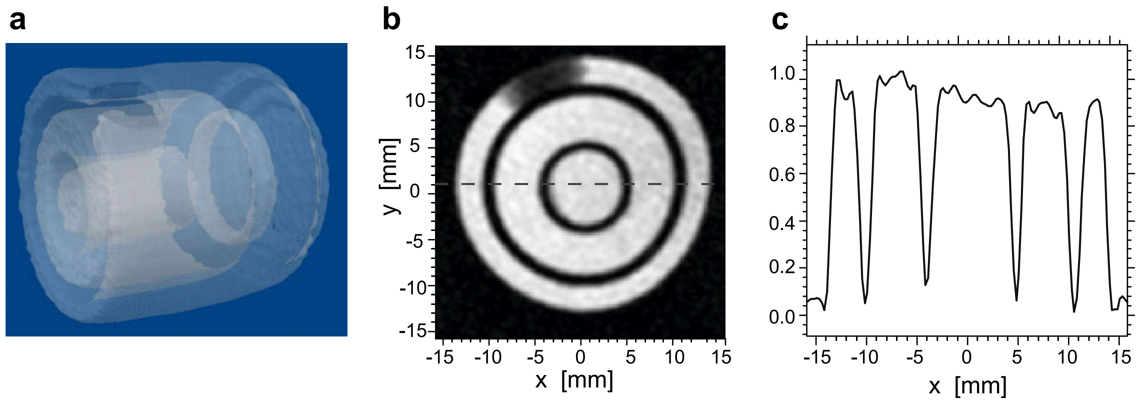

Fig. 8. (a) 3D image of a phantom sample composed of three concentric tubes filled with water. The FoV is 32 × 32 × 64 mm^3 with 64 × 64 × 32 pixels along each direction respectively. (b) 2D image of a slice of (a). (c) 1D profile of the 2D plot at the position marked by the grey line in (b). The experimental data were acquired during t_{acq} = 0.64 ms with a sampling rate of 10 μs, an echo time of t_E = 3 ms and with a recycling delay T_R = 6 s, and 4 scans. The final SNR in the image is about 60.

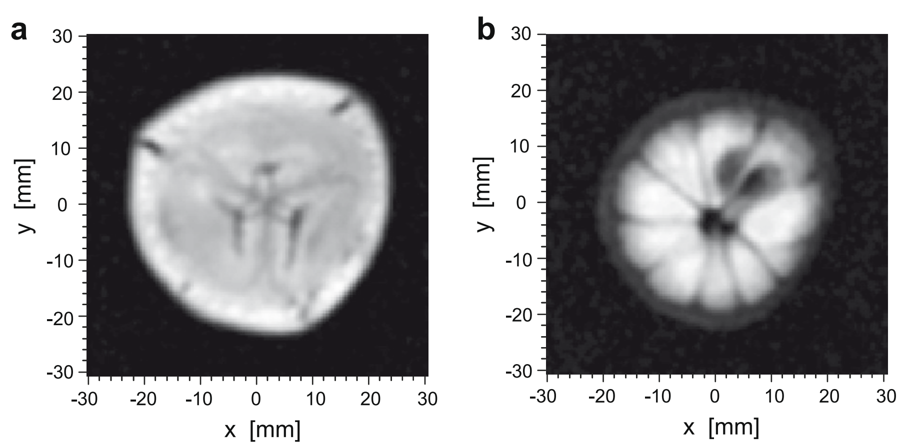

Fig. 9. Cross-section of a banana (a), and a lemon (b) measured with a field-of-view of 56 mm, 64 pixels along each direction, and selecting a slice 5 mm thick. The total measurement time was about 2 min.

centric tubes filled with water. Fig. 8b shows a slice through the same object. Besides resolving the concentric rings, the image shows a bubble in the outer water shell. The spatial resolution and sensitivity can be also appreciated in Fig. 8c, where a 1D profile along the line marked in gray in Fig. 8b is plotted.

Finally the Halbach tomograph was used to resolve the structure of some fruits, like a banana (Fig. 9a) and a lemon (Fig. 9b). The sequence of Fig. 6b was applied setting the FoV to 56 mm and sampling 64 pixels along the lateral directions (~1 mm in-plane resolution). The structure of both fruits can be clearly identified. For the lemon not only the individual sections are resolved but also the pits at two different sections can be observed. Although the region in the *xy* plane covered by both fruits exceeds the limits of the maps shown in Fig. 7a, the field deviations in this larger volume are still small to not produce appreciable distortions in images.

6. Conclusions

The construction of a mobile Halbach magnet for MRI was described with particular attention to the use of movable small permanent magnet blocks to shim the field inhomogeneities caused by inherent heterogeneity of the magnetic material and the inaccuracy in size and position of the pieces in the final array. By combining different movements of shim magnets it was possible to generate and control all shim terms up to order two, including linear (x, y, and z), quadratic (x^2-y^2 and $2z^2-x^2-y^2$), and cross terms (xy, zy, and xz). The implementation of this shim unit improves the homogeneity by up to more than two orders of magnitude, i.e. from about 20 KHz line-width to values lower than 0.1 KHz, in samples with a diameter 1/10 of that of the total magnet. This degree of homogeneity allows the implementation of conventional imaging methods using readout gradients to obtain artifact-free 3D images in extremely short experimental times. Furthermore, such a reduction in the line-width strongly reduces the power requirement to the gradient amplifier, which is important in terms of portability. Finally, it was possible to recover proton spectral information from volumes as large as 1 cm^3, where sub ppm resolution was achieved. In contrast with previous works, where the strategy to obtain high resolution in portable magnets consisted of reducing the sample volume using micro coils [4,6,7,21–23], the shimming technique described in this paper allowed us to achieve relatively good homogeneity in a magnet volume fraction (sample volume/magnet volume) several orders of magnitude larger than those previously reported. By including variables of control in other magnet geometries, like the one described in [22] is expected to help correcting the field inhomogeneities (mainly of first and second order) allowing to use larger samples or to achieve better homogeneity, factors that would lead to important SNR improvements.

Acknowledgement

This project was supported by the Deutsche Forschungsgemeinschaft, grant CA660/1-1, "Development of methodologies and portable sensors for high resolution NMR spectroscopy in inhomogeneous fields". Ernesto Danieli thanks the Alexander von Humboldt Foundation for a research scientist Fellowship. We thank K. Kupferschläger for technical support.

References

[1] B. Blümich, NMR Imaging of Materials, Clarendon Press, Oxford, 2000.
[2] B. Blümich, J. Perlo, F. Casanova, Mobile single-sided NMR, Progress in Nuclear Magnetic Resonance Spectroscopy 52 (2008) 197–269.
[3] K. Halbach, Design of permanent multipole magnets with oriented rare-earth cobalt material, Nuclear Instruments & Methods 169 (1980) 1–10.
[4] G. Moresi, R. Magin, Miniature permanent magnet for table-top NMR, Concepts in Magnetic Resonance Part B-Magnetic Resonance Engineering 19B (2003) 35–43.
[5] H. Raich, P. Blümler, Design and construction of a dipolar Halbach array with a homogeneous field from identical bar magnets: NMR Mandhalas, Concepts in Magnetic Resonance Part B-Magnetic Resonance Engineering 23B (2004) 16–25.
[6] B.P. Hills, K.M. Wright, D.G. Gillies, A low-field, low-cost Halbach magnet array for open-access NMR, Journal of Magnetic Resonance 175 (2005) 336–339.
[7] R.C. Jachmann, D.R. Trease, L.S. Bouchard, D. Sakellariou, R.W. Martin, R.D. Schlueter, T.F. Budinger, A. Pines, Multipole shimming of permanent magnets using harmonic corrector rings, Review of Scientific Instruments 78 (2007) 035115.
[8] S. Anferova, V. Anferov, J. Arnold, E. Talnishnikh, M.A. Voda, K. Kupferschlager, P. Blümler, C. Clauser, B. Blümich, Improved Halbach sensor for NMR scanning of drill cores, Magnetic Resonance Imaging 25 (2007) 474–480.
[9] J. Perlo, V. Demas, F. Casanova, C.A. Meriles, J. Reimer, A. Pines, B. Blümich, High-resolution NMR spectroscopy with a portable single-sided sensor, Science 308 (2005) 1279.
[10] J. Perlo, F. Casanova, B. Blümich, Ex situ NMR in highly homogeneous fields: H-1 spectroscopy, Science 315 (2007) 1110–1112.
[11] J.A. Jackson, Classical Electrodynamics, John Wiley & Sons, New York, 1999.
[12] M.J.E. Golay, Field homogenizing coils for nuclear spin resonance instrumentation, Review of Scientific Instruments 29 (1958) 313–315.
[13] E.P. Danieli, J. Perlo, F. Casanova, B. Blümich, High-performance shimming with permanent magnets, in: S.L. Codd, J.D. Seymour (Eds.), Spatially Resolved NMR Techniques and Applications, Wiley-VCH, Weinheim, 2009, pp. 487–499.
[14] P. Blümler, The NMR-Cuff: Force Free, Hinged Magnet Arrangements For Portable MRI and EPR, ICMRM9, Aachen, Germany, 2007.
[15] P. Callaghan, Principles of Nuclear Magnetic Resonance Microscopy, Clarendon Press, Oxford, 1991.
[16] A.A. Maudsley, H.E. Simon, S.K. Hilal, Magnetic-field measurements by NMR imaging, Journal of Physics E-Scientific Instruments 17 (1984) 216–220.
[17] F. Romeo, D.I. Hoult, Magnetic field profiling – analysis and correcting coil design, Magnetic Resonance in Medicine 1 (1984) 44–65.
[18] G.N. Chmurny, D.I. Hoult, The ancient and honourable art of shimming, Concepts in Magnetic Resonance 2 (1990) 131–149.
[19] P. Jezzard, R.S. Balaban, Correction for geometric distortion in echo-planar images from B_0 field variations, Magnetic Resonance in Medicine 34 (1995) 65–73.
[20] J. Weis, U. Gorke, R. Kimmich, Susceptibility, field inhomogeneity, and chemical shift-corrected NMR microscopy: application to the human finger in vivo, Magnetic Resonance Imaging 14 (1996) 1165–1175.
[21] V. Demas, J.L. Herberg, V. Malba, A. Bernhardt, L. Evans, C. Harvey, S.C. Chinn, R.S. Maxwell, J. Reimer, Portable, low-cost NMR with laser-lathe lithography produced microcoils, Journal of Magnetic Resonance 189 (2007) 121–129.
[22] A. McDowell, E. Fukushima, Ultracompact NMR: H-1 spectroscopy in a subkilogram magnet, Applied Magnetic Resonance 35 (2008) 185–195.
[23] A.F. McDowell, N.L. Adolphi, Operating nanoliter scale NMR microcoils in a 1 tesla field, Journal of Magnetic Resonance 188 (2007) 74–82.